

# INLET BOUNDARY CONDITIONS FOR EMBEDDED LES

Lars Davidson

Division of Fluid Dynamics, Department of Applied Mechanics  
Chalmers University of Technology, SE-412 96 Göteborg, Sweden  
<http://www.tfd.chalmers.se/~lada>, [lada@chalmers.se](mailto:lada@chalmers.se)

## ABSTRACT

The paper evaluates a new method to prescribe synthesized turbulent inlet boundary conditions. The method can also be used when prescribing turbulent fluctuations at an interface between (U)RANS and LES regions when the flow enters the LES region. When making LES, DES or hybrid LES-RANS a precursor channel DNS is often used. The disadvantage of this method is that it is difficult to re-scale the DNS fluctuations to higher Reynolds numbers. In the present work synthesized isotropic turbulent fluctuations are generated at the inlet plane with a prescribed turbulent length scale and energy spectrum. A large number of independent realizations are generated. A correlation in time between these realizations is introduced via an asymmetric, non-truncated time filter. In this way the turbulent time scale of the synthesized isotropic turbulent fluctuations is prescribed.

The method has previously been validated for DNS channel flow at  $Re_\tau = 500$  [1]. In that study it was found that the present approach is at least as good as using inlet boundary conditions from a pre-cursor DNS. It is employed in the present study in hybrid LES-RANS of the flow around a three-dimensional hill and the flow over the downstream part of a bump. The sensitivity to the strength (amplitude) of the inlet fluctuations is investigated.

Most of the bump simulations include only a central slice of the domain. One simulation was also carried out in which the sidewalls are included, which creates strong secondary flow.

## 1 INTRODUCTION

Isotropic synthesized fluctuations based on the method of Kraichnan [2] are often used to generate turbulent fluctuations. This method prescribes an energy spectrum that yields the amplitude of the fluctuations as a function of wave number. Non-isotropic fluctuations have been investigated [3–7] where the fluctuations were scaled so that the time-averaged synthesized fluctuations match a prescribed Reynolds stress tensor. A disadvantage of this kind of scaling is that the prescribed spectrum, and hence the two-point correlation, are modified if – as is always the case in real flows – the Reynolds stress ten-

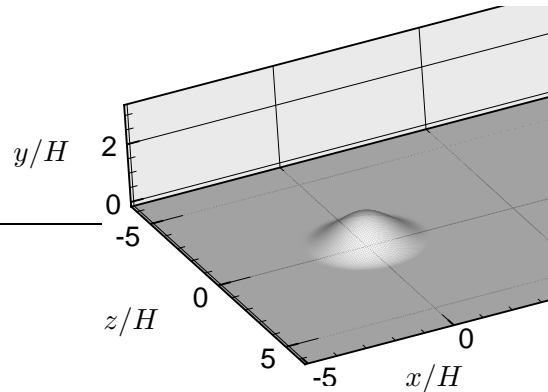


Figure 1: 3D hill. Computational domain. Hill crest at  $x = z = 0$ . Extension of hill:  $-2 \leq x/H \leq 2$ ;  $-2 \leq z/H \leq 2$ . Inlet and outlet located at  $x/H = -4.1$  and  $x/H = 15.4$ , respectively.

sor is non-homogeneous.

To achieve correlation in time, Fourier series were applied in time in the same way as in space in most of the work cited above. In [8] a method was also investigated where a three-dimensional box with generated fluctuations was convected across the inlet plane; in this way fluctuation correlations in the streamwise directions were transformed into correlations in time. In the work by Billson *et al.* [6] correlation in time is defined by an asymmetric infinite time filter. The method offers a convenient way to prescribe turbulent length and time scales independently. This method is adopted in the present work.

A method based partly on synthesized fluctuations was recently presented and is called the vortex method [9]. It is based on a superposition of coherent eddies where each eddy is described by a shape function that is localized in space. The eddies are generated randomly in the inflow plane and then convected through it. The method is able to reproduce first and second-order statistics as well as two-point correlations.

## 2 SYNTHESIZED TURBULENCE

A turbulent velocity field can be simulated using random Fourier modes. The velocity field is given by  $N$

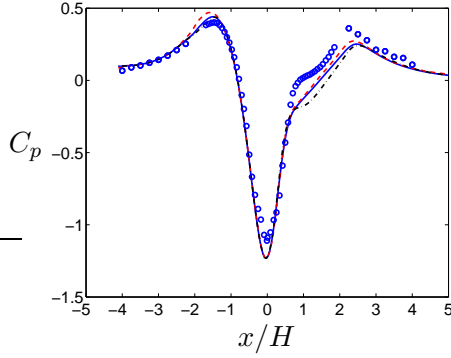


Figure 2: 3D hill. Pressure coefficient.  $z = 0$ .  
 --- :  $u_{rms,in}/u_\tau = 0.5$ ; — :  $u_{rms,in}/u_\tau = 1$ ; - · - :  
 $u_{rms,in}/u_\tau = 2$ ; markers: experiments [10].

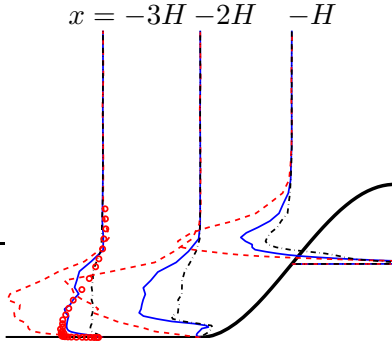


Figure 3: 3D hill. Resolved shear stresses.  $z = 0$ .  
 --- :  $u_{rms,in}/u_\tau = 0.5$ ; — :  $u_{rms,in}/u_\tau = 1$ ; - · - :  
 $u_{rms,in}/u_\tau = 2$ ; markers: experiments [10].

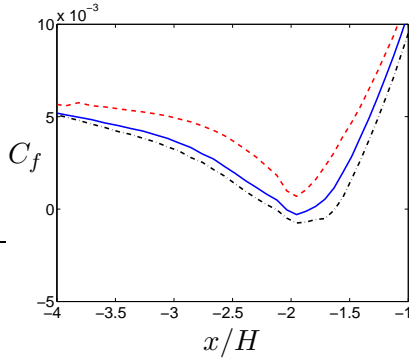


Figure 4: 3D hill. Friction coefficient.  $z = 0$ . --- :  
 $u_{rms,in}/u_\tau = 0.5$ ; — :  $u_{rms,in}/u_\tau = 1$ ; - · - :  
 $u_{rms,in}/u_\tau = 2$ .

random Fourier modes as

$$(1) \quad u'_i(x_j) = 2 \sum_{n=1}^N \hat{u}^n \cos(\kappa_j^n x_j + \psi^n) \sigma_i^n$$

where  $\hat{u}^n$ ,  $\psi^n$  and  $\sigma_i^n$  are the amplitude, phase and direction of Fourier mode  $n$ . The highest wave number is defined on the basis of mesh resolution  $\kappa_{max} = 2\pi/(2\Delta)$ . The smallest wave number is defined from  $\kappa_1 = \kappa_e/p$ , where  $\kappa_e$  corresponds to the energy-carrying eddies. Factor  $p$  should be larger

than one to make the largest scales larger than those corresponding to  $\kappa_e$ . In the present work  $p = 2$ . The wavenumber space,  $\kappa_{max} - \kappa_1$ , is divided into  $N = 600$  modes, equally large, of size  $\Delta\kappa$ . A modified von Kármán spectrum is chosen. The amplitude of the fluctuations is set so that RMS is equal to a factor,  $\gamma$ , multiplied by the friction velocity at the inlet, i.e.  $u_{rms,in} = v_{rms,in} = w_{rms,in} = \gamma u_{\tau,in}$ . The value of  $\gamma$  is set to 0.5, 1 or 2.

A fluctuating velocity field is generated each time step as described above. They are independent of each other, however, and their time correlation will thus be zero. This is unphysical. To create correlation in time, new fluctuating velocity fields,  $\mathcal{U}'_i$ , are computed based on an asymmetric time filter.

$$(2) \quad (\mathcal{U}'_i)^m = a(\mathcal{U}'_i)^{m-1} + b(u'_i)^m$$

where  $m$  denotes the time step number and  $a = \exp(-\Delta t/T)$ . This asymmetric time filter resembles the spatial digital filter presented by Klein *et al.* [11]. The second coefficient is taken as  $b = (1 - a^2)^{0.5}$  which ensures that  $\langle \mathcal{U}'_i{}^2 \rangle = \langle u_i'^2 \rangle$  ( $\langle \cdot \rangle$  denotes averaging). The time correlation of  $\mathcal{U}'_i$  will be equal to  $\exp(-\Delta t/T)$ , and thus Eq. 2 is a convenient way to prescribe the turbulent time scale of the fluctuations. The inlet boundary conditions are prescribed as

$$(3) \quad \bar{u}_i(0, y, z, t) = U_{i,in}(y) + u'_{i,in}(y, z, t)$$

where  $u'_{i,in} = (\mathcal{U}'_i)^m$  and  $U_{i,in}(y)$  denotes the mean inlet profile.

The turbulent length scale and time scale are  $L_t = 0.1$  and  $T_t = 0.05$ , respectively, scaled with the boundary layer thickness and the friction velocity at the inlet. The wavenumber,  $\kappa_e$ , is obtained as  $\kappa_e = \alpha 9\pi/(55L_t)$  with  $\alpha = 1.453$ .

The synthetic fluctuations created with the method presented above yield homogeneous turbulence in the inlet plane, i.e.  $u_{rms,in}$ ,  $v_{rms,in}$ , and  $w_{rms,in}$  are constant (and equal) across the entire inlet plane. The fluctuations could of course be scaled so that their RMS follow some prescribed  $y$  variation but, as pointed out in [1], this would destroy the two-point correlations that have implicitly been prescribed via the von Kármán spectrum. However, the fluctuations must be reduced near the wall so that they go smoothly to zero as the wall is approached (this is done for  $y/\delta_{in} \lesssim 0.004$ ).

The synthetic fluctuations must also be modified in some way at the outer edge of the boundary layer. To achieve this, the fluctuations are multiplied by a blending function

$$(4) \quad f_{bl} = \max\{0.5[1 - \tanh(n - \delta_{in})/b], 0.1\}$$

where  $n$  is the distance to the closest wall and  $b$  is the distance over which  $f_{bl}$  goes from 1 to 0. Freestream turbulence is prescribed by not letting  $f_{bl}$  become smaller than 0.1.

### 3 THE NUMERICAL METHOD

An incompressible, finite volume code is used [12]. For space discretization, central differencing is used for all terms in the momentum equations. Upwind differencing is used for the convective terms in the equation for the turbulent kinetic energy,  $k_T$ . The Crank-Nicolson scheme (with  $\alpha = 0.5$  for the convective and diffusive terms) is used for time discretization of all equations. Slightly higher  $\alpha$ , i.e. slightly more implicit time discretization, is used for the pressure gradient in order to ensure stability;  $\alpha_p = 0.6$  is used for the 3D hill flow and  $\alpha_p = 0.75$  is used for the bump simulations.

The numerical procedure is based on an implicit, fractional step technique with a multigrid pressure Poisson solver [13] and a non-staggered grid arrangement.

### 4 THE HYBRID LES-RANS MODEL

Hybrid LES-RANS is used. A one-equation for the modelled turbulent kinetic energy,  $k_T$ , is solved in the entire domain. URANS is employed near the wall and LES is used in the remaining part of the domain. The only difference between the two regions is the definition of the length scale when computing the turbulent viscosity and the dissipation term in the  $k_T$  equation. The length scale in the URANS is proportional to the wall distance whereas in the LES region it is taken as the cell volume up to the power of  $1/3$ . For more detail, see [14]; no forcing is used at the interface.

### 5 RESULTS

In both test cases three different RMS amplitudes of the inlet fluctuations are investigated:  $u_{rms,in}/u_\tau = 0.5, 1$  and  $2$ . The three cases are denoted Case  $u_\tau/2$ ,  $u_\tau$  and  $2u_\tau$ , respectively. To ensure numerical stability, Neumann boundary conditions are used at the outlets instead of convective boundary conditions.

#### 5.1 3D hill flow

A  $162 \times 82 \times 130$  ( $x, y, z$ ) mesh is used (1.7 million cells). The Reynolds number is 130 000 based on the hill height. The height of the domain is  $3.2H$ , see Fig. 1 The inlet boundary layer thickness is  $\delta_{in}/H = 0.5$  at both the lower and upper wall. The grid resolutions at the inlet expressed in wall units are  $\Delta x^+ = 280$  and  $\Delta z^+ = 120$ , which correspond to  $\Delta x/\delta_{in} = 0.12$  and  $\Delta z/\delta_{in} = 0.051$ , respectively. The first near-wall cell center is located at  $y^+ = 1.5$ . The matching line is defined along an instantaneous streamline; for more detail, see [15]. The time step is  $9.3 \cdot 10^{-4} U_{in}/H$ . This gives a maximum instantaneous CFL number of approximately 2.3 which occurs in the wall-normal direction; the maximum CFL number in the streamwise direction is approximately 0.75. Averaging was performed over approximately 30 000 time steps.

Figures 2 and 3 present the surface pressure over

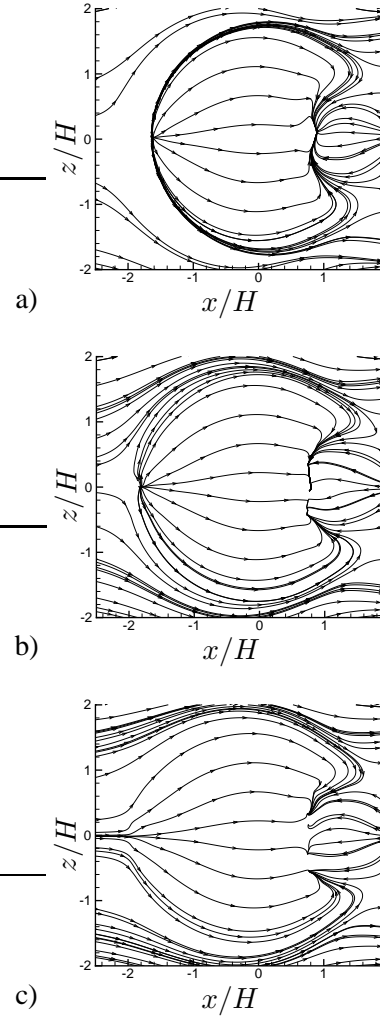


Figure 5: 3D hill. Streamtraces at the lower wall,  $z = 0$ . a)  $u_{rms,in}/u_\tau = 0.5$ . b)  $u_{rms,in}/u_\tau = 1$ . c)  $u_{rms,in}/u_\tau = 2$

the hill and the resolved shear stresses on the wind-side of the hill, respectively. As can be seen, the fluctuations in Case  $2u_\tau$  seem to be too strong; an overshoot is seen in the pressure coefficient at  $x/H = -1.5$  and the magnitude of the resolved shear stresses is too large. On the other hand, for Case  $u_\tau/2$ , the inlet fluctuations seem to be too small since only small resolved stresses are generated at  $x/H = -3$ . No difference is seen in the pressure coefficient between cases  $u_\tau/2$  and  $u_\tau$ . Because only small resolved stresses are created for Case  $u_\tau/2$ , the skin friction (Fig. 4) is consequently smaller than for Case  $u_\tau$ , which in turn is smaller than for Case  $2u_\tau$ . A small recirculation bubble is also formed at the foot ( $x/H \simeq -2$ ) of the hill for Case  $u_\tau/2$ , which is not the case the other two cases.

Because the computed flow at the foot of the windside of hill is fairly different for the three cases, the flow over the hill is also different. The stream traces on the lower wall are presented in Fig. 5. As

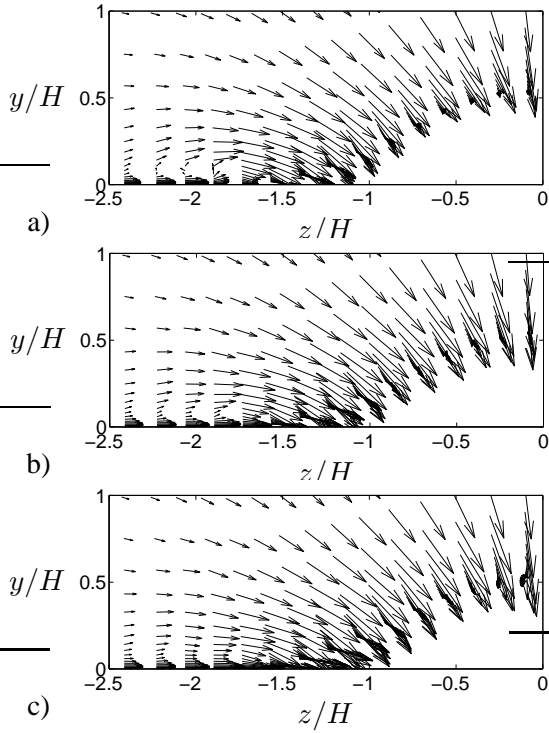


Figure 6: 3D hill. Velocity vectors at  $x = H$ . Every 2nd (3rd) vector plotted in the  $y$  ( $z$ ) coordinate direction. a)  $u_{rms,in}/u_\tau = 0.5$ . b)  $u_{rms,in}/u_\tau = 1$ . c)  $u_{rms,in}/u_\tau = 2$ .

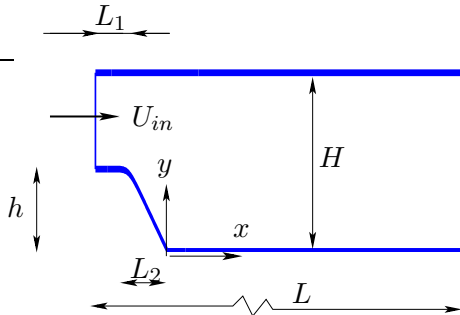


Figure 7: Onera bump. Computational domain (not to scale).

can be seen, in Case  $u_\tau/2$ , the flow diverges laterally towards the sides of the hill because of deceleration of the flow in the center region due to the small recirculation bubble. Because of the differences in the flow at the windside of the flow, differences are also found on the leeside.

Traces of the recirculating bubble formed at the wind-side for Case  $u_\tau/2$  can also be seen at  $x = H$  in Fig. 6b at  $(y/H, z/H) = (0.05, -1.8)$ .

## 5.2 Onera bump: slice

Measurements were carried out by ONERA in the DESider project [16].  $Re_h = 0.93 \cdot 10^6$  based on the bump height,  $h$ . The rectangular duct has the following dimensions (see Fig. 7):  $W/H = 1.67$ ,  $h/H =$

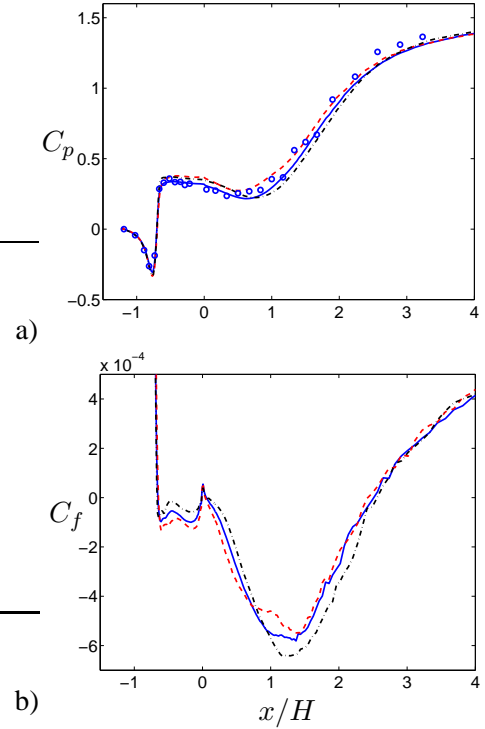


Figure 8: Onera bump. --- :  $u_{rms,in}/u_\tau = 0.5$ ; — :  $u_{rms,in}/u_\tau = 1$ ; -.- :  $u_{rms,in}/u_\tau = 2$ ; markers: experiments [16]. Lower wall. a) Pressure coefficient; b) friction coefficient.

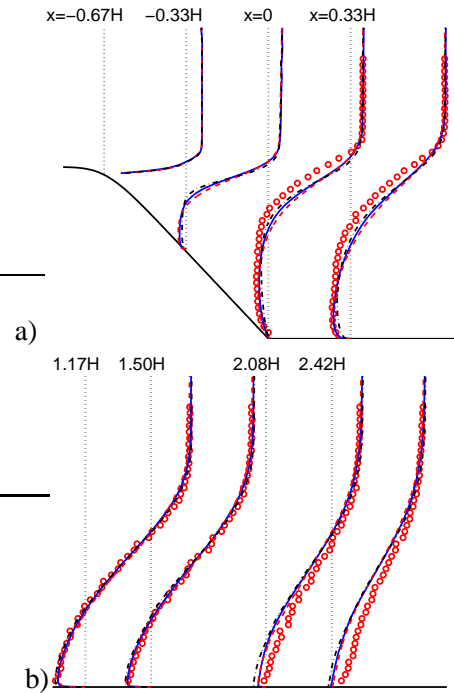


Figure 9: Onera bump. Streamwise mean velocity profiles,  $\langle \bar{u} \rangle / U_b$ . --- :  $u_{rms,in}/u_\tau = 0.5$ ; — :  $u_{rms,in}/u_\tau = 1$ ; -.- :  $u_{rms,in}/u_\tau = 2$ ; markers: experiments [16].

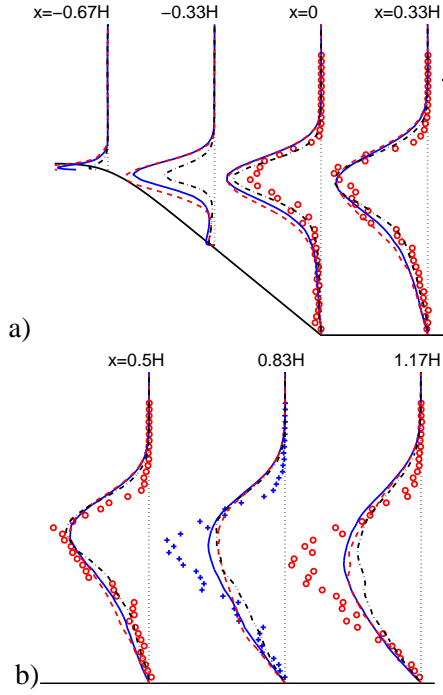


Figure 10: Onera bump. Resolved shear stresses. ---:  $u_{rms,in}/u_\tau = 0.5$ ; —:  $u_{rms,in}/u_\tau = 1$ ; - - -:  $u_{rms,in}/u_\tau = 2$ ; markers: experiments [16].

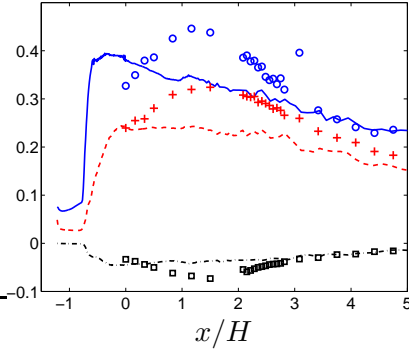


Figure 11: Onera bump. Peak resolved fluctuations. —, circle:  $u_{rms}/U_b$ ; - - -, plus:  $v_{rms}/U_b$ ; - - -, square:  $\langle u'v' \rangle / U_b^2$ ; markers: experiments [16].

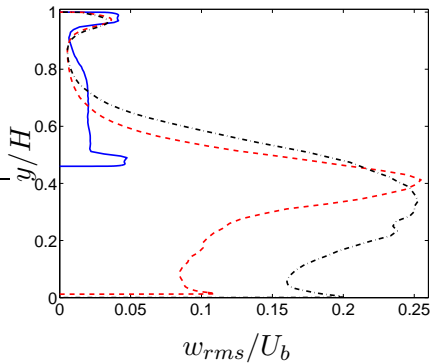


Figure 12: Onera bump. Spanwise resolved fluctuations. —:  $x/H = -1$ ; - - -:  $x/H = 0$ ; - - -:  $x/H = 1.2$ .

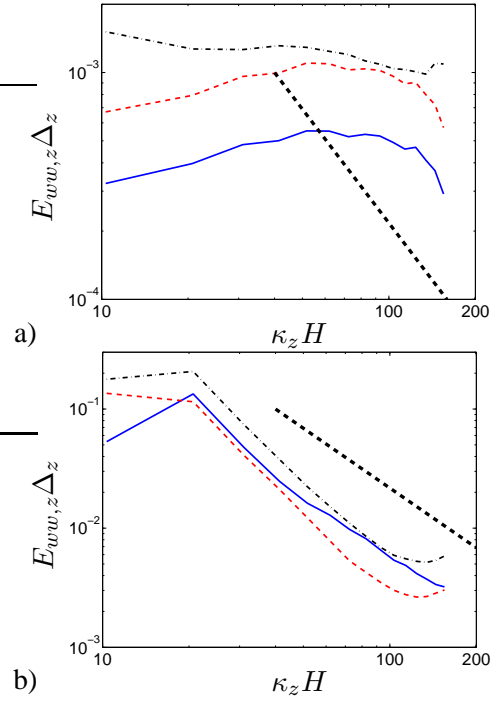


Figure 13: Onera bump. Energy spectra  $E_{ww}(\kappa_z)$ .  $u_{rms,in}/u_\tau = 1$ . Thick dashed line shows the  $-5/3$  slope. a)  $x/H = -1$ . —:  $(y - y_{wall})/H = 0.00025$ ; - - -:  $(y - y_{wall})/H = 0.0019$ ; - - -:  $(y - y_{wall})/H = 0.03$  (location of maximum  $w_{rms}$ ). b)  $x/H = 1.2$ . —:  $y/H = 0.0035$  (location of inner local maximum of  $w_{rms}$ ); - - -:  $y/H = 0.13$ ; - - -:  $y/H = 0.34$  (location of maximum  $w_{rms}$ ).

0.46,  $L_1/H = 0.41$ ,  $L_2/H = 0.81$ ,  $H = 0.3m$ . The inlet boundary layer thickness is  $\delta_{in}/H = 0.043$ . In this subsection, simulations of the Onera bump were carried out using only a slice in the central region and periodic boundary conditions in the spanwise direction. The extent of the domain in the spanwise direction is  $-0.61/2 \leq z/H \leq 0.61/2$  and total length in the streamwise direction is  $L/H = 8.86$ . 32 cells are used in the  $z$ -direction ( $\Delta z/H = 0.019$ ,  $\Delta z/\delta_{in} = 0.44$ ). The grid in the  $x - y$  plane has  $224 \times 120$  cells. At the inlet  $\Delta x/H = 0.014$  ( $\Delta x/\delta_{in} = 0.33$ ); for  $0 \leq x/H \leq 1$  we have  $\Delta x/H = 0.018$ . In wall units this yields  $\Delta x^+ = 1300$  and  $\Delta z^+ = 1800$  at the inlet. The matching plane between LES and URANS is prescribed along fixed grid planes; the URANS region near the upper and the lower walls extends 12 wall-adjacent cells. The mean inlet boundary conditions are taken from URANS simulations of the entire bump using a zonal version of the Reynolds stress- $\omega$  model [17]; in the slice region the results of the URANS simulations match the experimental data.

The time step is  $4.2 \cdot 10^{-4}s = 5.0 \cdot 10^{-3}U_b/H$  where  $U_b$  denotes the bulk velocity downstream of the bump. This gives a maximum instantaneous CFL number of approximately 2.3, which occurs in the

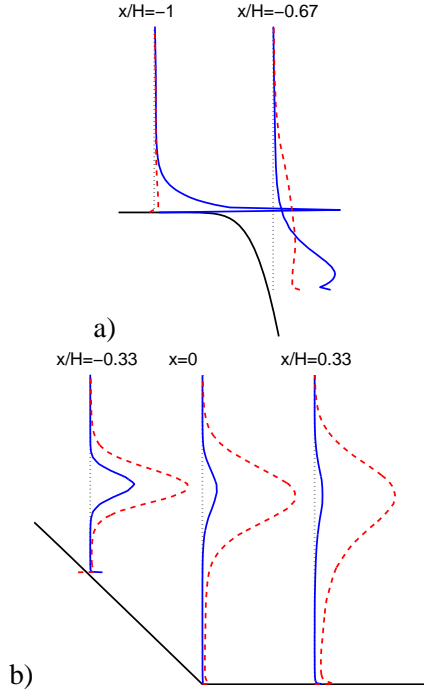


Figure 14: Onera bump.  $u_{rms,in}/u_\tau = 1$ . SGS dissipations. Note that different scalings are used in a) and b). — :  $\varepsilon_{SGS}$ ; - - - :  $\varepsilon'_{SGS}$  (see Eq. 5). a)  $\max(\varepsilon_{SGS,mean}) = 190$  at  $x/H = -1$ ; b)  $\max(\varepsilon'_{SGS}) = 17$  at  $x/H = -0.33$ .

wall-normal direction; the maximum CFL number in the streamwise direction is approximately 0.75. Averaging was performed over more than 30 000 time steps and, of course, in the spanwise direction.

The Reynolds number for this flow is an order of magnitude larger than for the 3D hill, and the boundary layer is much thinner. Thus the grid is very coarse, expressed in both inner and outer scaling. This makes it a very demanding test case. Note, however, that this kind of resolution is relevant from an industrial point of view.

Figure 8 shows the pressure coefficient and the skin friction along the lower wall. As can be seen, the agreement with the experimental pressure coefficient is good for all three cases, at least up to  $x/H = 2$ ; the skin friction coefficient at  $x/H \simeq 1$  indicates that the strength of the backflow increases with a decreasing amplitude of the inlet fluctuations (this is also visible when zooming in on the velocity profile at  $x/H = 1.17$ ). Further downstream, the pressure coefficients indicate that the experimental flow recovers faster than the predicted flow, which is also seen by looking at the velocity profiles in Fig. 9. Although the resolved shear stresses agree fairly well with experiments for  $x/H \leq 0.5$ , see Fig. 10, the peak value in the experimental stresses increases for  $0.5 < x/H < 1.5$ , whereas the peak value of the predicted stresses stays fairly constant. This is also seen in Fig. 11 where the peak fluctu-

ations are plotted versus  $x$ . It can be seen that the maximum experimental stresses occur further downstream (at  $x/H = 1.5$ ) compared to predictions, and also that the experimental peak is more pronounced than in the predictions. This explains why the experimental recovery rate is much faster than the predicted one. It is found that the experimental shear stresses increase by some 20% between  $x/H = 0.5$  and  $x/H = 0.83$ . At  $x/H = 1.5$  the peak is 50% larger than at  $x/H = 0.5$ ; it then starts to decay. The reason for the discrepancy in shear stresses is probably three-dimensional effects (recall that the side walls are not included in the simulations). Secondary streamwise vortices are created near the side walls, and it may be that at  $x/H = 0.5$  their influence reaches all the way to the centerplane; note, however, that the predicted velocity profiles agree well with experiments all the way up to  $x/H = 1.50$ . For larger  $x$ , the too small shear stresses start to affect the predicted velocity profiles.

In Fig. 10a it can be seen that, for Case  $u_\tau/2$ , only very small resolved fluctuations are created for  $x/H \leq -0.67$ . The peak is approximately 40% of that for Case  $u_\tau$ . The peak for Case  $2u_\tau$  is 50% larger than that for Case  $u_\tau$ . For Case  $u_\tau/2$  the resolved fluctuations are still too small at  $x/H = -0.33$ . The magnitudes in the resolved shear stresses are also reflected in the skin frictions in Fig 8: high resolved shear stress gives large skin friction and vice versa. The point separation is consequently also affected: high resolved shear stress pushes the separation point further downstream and vice versa.

The one-dimensional spectra are presented in Fig. 13 at two streamwise locations, at  $x/H = -1$  (close to the inlet) and at  $x/H = 1.2$  (in the recirculation region). The smallest wavenumber is  $\kappa_{z,min} = 2\pi/z_{max}$ . The largest wavenumber included in the plots is  $\kappa_{z,max} = 2\pi/2\Delta z$ , where we have assumed that two cells are required to resolve a wavelength. This gives  $\kappa_{z,min} = 2\pi/(0.61H) = 10/H$  and  $\kappa_{z,max} = \pi/(0.019H) = 165/H$ . The spectra are shown for three  $y$  locations at each streamwise position. In Fig. 13a one point is near the wall, one at the location of maximum  $w_{rms}$  (see Fig. 12) and one point near the edge of the boundary layer. The grid near the inlet is – as previously mentioned – very coarse and as a result the turbulence is poorly resolved, as evidenced by the spectra in Fig. 13a. However, it can be seen in Fig. 12 that the level of the resolved turbulence is not unreasonably low because  $w_{rms,max}/u_\tau \simeq 0.9$ .

The spectra presented in Fig. 13b, on the other hand, appear to be physical reasonable. They all exhibit a  $-5/3$  range. Spectra are shown for three points, and the first point is located at the local inner maximum of  $w_{rms}$  ( $y/H = 0.0035$ ), see Fig. 12. The second point is located at  $y/H = 0.13$  and the

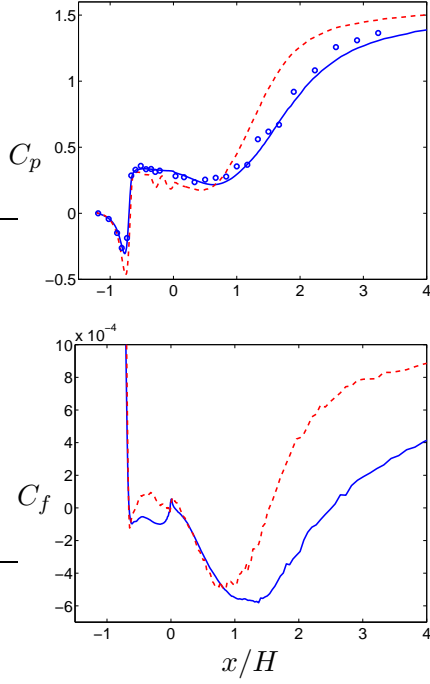


Figure 15: Onera bump. — : slice; - - - : full duct. a) Pressure coefficient; b) friction coefficient.

outermost point is located at  $y/H = 0.34$ , which is the location of the maximum of  $w_{rms}$  (that is in the shear layer).

We will next investigate the SGS dissipation, which reads

$$\varepsilon_{SGS} = 2\langle \nu_T \bar{s}_{ij} \bar{s}_{ij} \rangle$$

This is due to the instantaneous *total* strain rates,  $\partial \bar{u}_i / \partial x_j$ . The SGS dissipation due to the mean flow and the resolved fluctuations read, respectively,

$$(5) \quad \begin{aligned} \varepsilon_{SGS,mean} &= 2\langle \nu_T \rangle \langle \bar{s}_{ij} \rangle \langle \bar{s}_{ij} \rangle \\ \varepsilon'_{SGS} &= \varepsilon_{SGS} - \varepsilon_{SGS,mean} \end{aligned}$$

Figure 14 presents SGS dissipations. The SGS dissipation due to the time-averaged mean flow is very large near the inlet ( $x/H = -1$ ). This is because the resolution is very poor. Further downstream, the SGS dissipation is dominated by resolved fluctuations as the grid resolution becomes relevant for resolving a large part of the energy spectrum, see Fig. 13b.

### 5.3 Onera bump: full duct

In this subsection we compute the flow in the full duct. The mesh in the  $x - y$  plane is identical to that used in the slice simulations. The number of cells in the spanwise direction is 152. Constant grid spacing ( $\Delta z/H = 0.019$ ) is used for  $-0.61/2 \leq z/H \leq 0.61/2$ , which is the same as in the slice simulations. The grid is compressed close to the

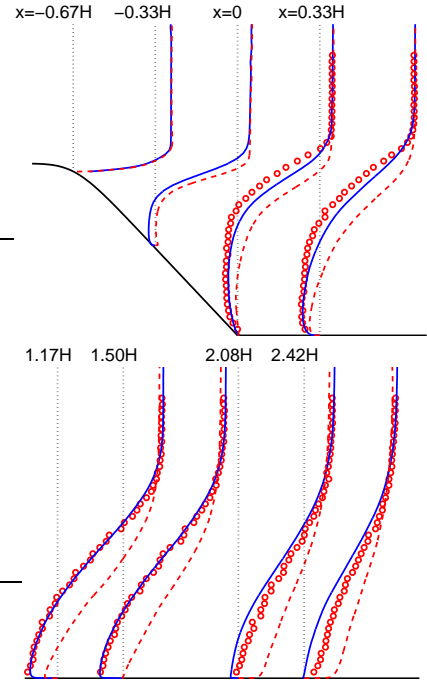


Figure 16: Onera bump. Streamwise mean velocity profiles. markers: experiments [16]. — : slice; - - - : full duct.

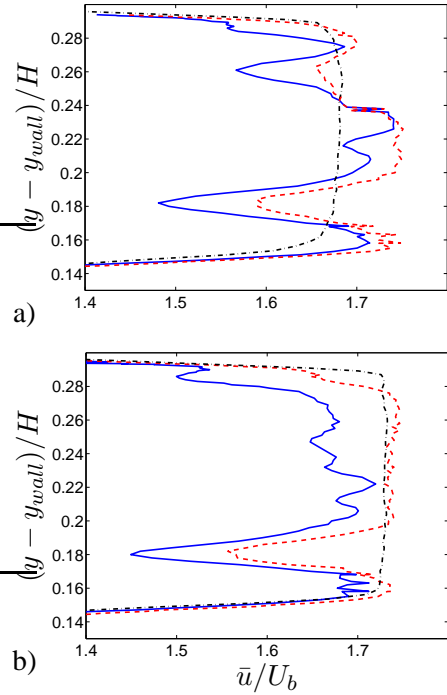


Figure 17: Onera bump. Inlet streamwise mean velocity profiles. Experiments [16]. a) — : experiments,  $z/H = -0.80$ ; - - - : experiments,  $z/H = -0.78$ ; - . - : simulations,  $z/H = -0.80$ . b) — : experiments,  $z/H = 0.80$ ; - - - : experiments,  $z/H = 0.78$ ; - . - : simulations,  $z/H = 0.78$ .

walls so that the first wall-adjacent nodes are located at approximately one viscous unit away from

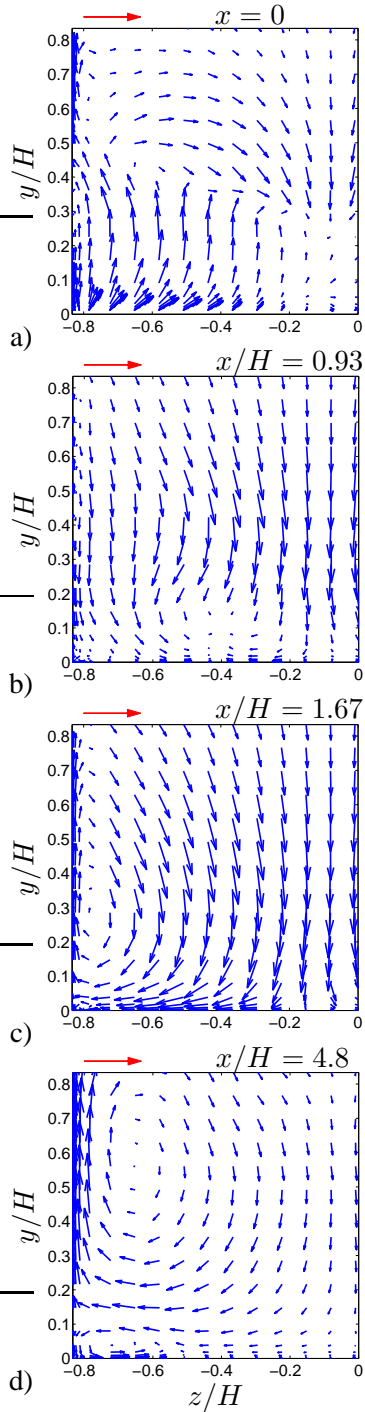


Figure 18: Onera bump. Secondary velocity vector fields. Simulations. Only every fourth vector in each direction is shown to enhance visibility. The vector on top of each plot shows the velocity vector  $W = 0.25U_b$ .

the wall. The amplitude of the inlet fluctuations is set to  $u_{rms}/u_\tau = 1$  and the blending function,  $f_{bl}$  (see Eq. 4), is used also at the lateral walls to dampen the inlet fluctuations from  $u_{rms}/u_\tau = 1$  in the boundary layers near the lateral walls to 0.1 in the central region. The extent of the URANS regions is defined by the first 12 cells. The time step was

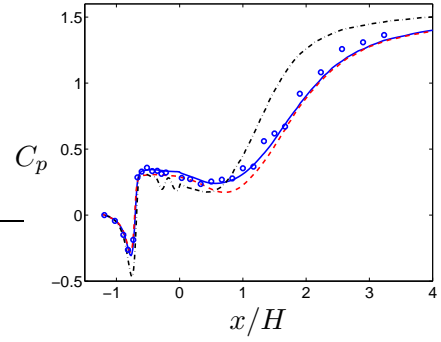


Figure 19: Onera bump. Pressure coefficients. — : Slice simulations,  $\Delta z/H = 0.019$ ; - - - : slice simulations,  $\Delta z/H = 0.0095$ . . . . : full-duct simulations.

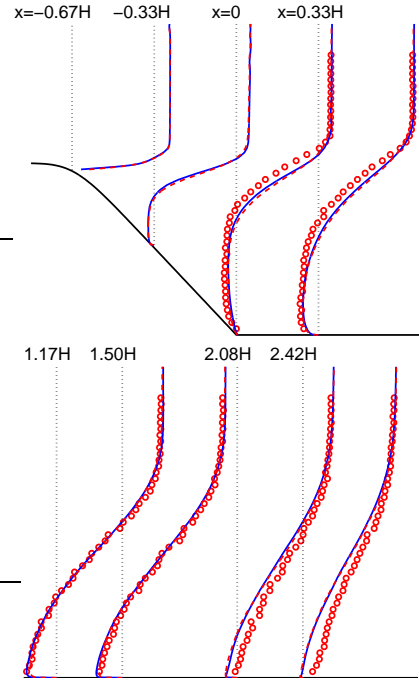


Figure 20: Onera bump. Streamwise mean velocity profiles. markers: experiments [16]. — : slice with  $\Delta z/H = 0.019$ ; - - - : slice with  $\Delta z/H = 0.0095$ .

$4.2 \cdot 10^{-4} s = 5.0 \cdot 10^{-3} U_b/H$ . This gives large instantaneous CFL numbers (up to 25); the large CFL numbers are created by the secondary flow in the lower corners of the duct. The maximum CFL number in the streamwise direction is close to one, and the maximum CFL number in the LES region is close to three. Averaging was performed over 42 000 time steps

Figures 15 and 16 present the pressure coefficient, the skin friction and the streamwise velocity profiles. As can be seen the full duct simulations give a recirculation bubble much smaller than both the experiments and the slice simulations. The former yields a recirculation bubble that extends to approximately  $x/H = 1.5$  whereas that of the latter extends to approximately  $x/H = 2.4$ . The extent

of the recirculation bubble of the full-duct simulations agrees well with the corresponding simulations of [18].

As mentioned above, the inlet conditions were taken from URANS simulations of the entire bump. One reason why the inlet conditions were not taken from the experimental profiles is that the experimental flow seems to include some secondary vortices on the bump, see Fig. 17. As can be seen, the streamwise velocity profiles close to the sidewalls exhibit velocity deficits close to the bump wall at  $(y - y_{wall})/H \simeq 0.18$  near both sidewalls. The inlet profiles taken from the URANS simulations are also included for  $z/H = -0.80$  and  $z/H = 0.78$  (recall that they are symmetric with respect to  $z = 0$ ). The experimental corner vortices are probably created far upstream in the resting tank, and since the resting tank was not included in the URANS simulations they were not captured in the simulations.

The predicted secondary flow field is shown for three cross-section planes in Fig. 18. As can be seen, the secondary flow is fairly strong, and this explains the differences between the slice and full duct simulations seen in Figs. 15 and 16. At the end of the bump ( $x = 0$ ) the secondary flow near the sidewall is directed upwards, but at  $x/H = 0.93$  – in the recirculation region – it is directed downwards. When the flow has re-attached, the flow along the sidewall again moves towards the lower wall and a clockwise vortex has formed with its center at  $(y/H, z/H) \simeq (0.77, 0.3)$ . Further downstream this vortex moves upwards and away from the wall (see Fig. 18d) and a new small counter-clockwise vortex is formed with its center located at  $(y/H, z/H) \simeq (0.05, -0.7)$ .

Now, why is there such a large discrepancy between the full-duct simulations and the experiments? One possibility is of course that the simulations are inaccurate. After all, the simulations are carried out using hybrid LES-RANS which involves a rather large element of modelling. Also, the time step may perhaps be too large. The CFL number for the secondary flow reaches disturbingly high levels (up to 25); however, in the LES region, the CFL number reaches “only” a value of 3. Still, as mentioned above, the large CFL numbers occur because of the secondary flow very close to the walls; the maximum instantaneous CFL number in the streamwise direction is actually smaller than one. **Figures 19 and 20 present pressure coefficients and velocity profiles for slice simulations where the number of cells in the spanwise direction has been doubled and, as can be seen, the fine spanwise resolution gives more or less identical results as the coarse one. From the skin friction (not shown), it is found that the predicted recirculation region is somewhat stronger with the fine resolution compared to the coarse one.**

## 6 CONCLUSIONS

The present study evaluates a novel approach for generating fluctuating turbulent inlet boundary conditions. Synthetic isotropic fluctuations are superimposed on a mean velocity profile. The synthesized fluctuations are created by assuming a modified von Kármán spectrum. The RMS of the fluctuations and their integral length scale are supplied as input when creating the von Kármán spectrum. A number of realizations (in this work 5000) of velocity fluctuations are generated in the inlet plane and stored on disk. Each realization corresponds to the inlet fluctuations at one time step. However, the 5000 realizations are independent, i.e. the time correlation of the prescribed inlet turbulent fluctuations is zero. This is unphysical. In order to introduce correlation in time, an asymmetric time filter is used. This filter includes a turbulent time scale, which is taken as  $0.1\delta_{in}/u_\tau$ .

Two flows are simulated in the present work, namely, the 3D hill flow and the flow over a bump. The results were obtained using different amplitudes on the fluctuating inlet conditions. It is found that the RMS amplitude of the inlet fluctuations should be close to one when scaled with the friction velocity at the inlet.

Coarse grids were purposely chosen since this is of high relevance for industrial flows. For the bump flow the inlet boundary layer is indeed very poorly resolved. The spanwise and streamwise grid spacing are 0.44 and 0.33, respectively, when scaled with the inlet boundary layer thickness and the corresponding resolutions in wall units are 1800 and 1300. Consequently, the spectra of the resolved fluctuations do not exhibit any physical realism. However, the resolved turbulence downstream of the bump exhibits clear  $-5/3$  ranges, both in the recirculation region and in the shear layer.

The SGS dissipation,  $\varepsilon_{SGS} = 2\langle\nu_T\bar{s}_{ij}\bar{s}_{ij}\rangle$ , is evaluated both in the boundary layer on the bump and downstream of the bump. It is found that, in the poorly resolved boundary layer, the SGS dissipation is created by the time-averaged flow, i.e. by  $\varepsilon_{SGS,mean} = 2\langle\nu_T\rangle\langle\bar{s}_{ij}\rangle\langle\bar{s}_{ij}\rangle$ . As we move further downstream, the SGS dissipation is progressively taken over by the resolved fluctuations, i.e. by  $\varepsilon'_{SGS} = \varepsilon_{SGS} - \varepsilon_{SGS,mean}$ . The relation between  $\varepsilon'_{SGS}$  and  $\varepsilon_{SGS,mean}$  seems to be a good measure of how much of the energy spectrum is resolved.

The bump in the experiments is placed in a duct. Most of the bump simulations were carried out in a computational domain covering only a slice in the middle, omitting the sidewalls. In the final part of the paper, the results of slice simulations were compared with full-duct simulations including the sidewalls. The grid used in the slice simulations is identical to the corresponding region of that used in the full-duct simulations. It is found that the former results agree much better with the experiments than the

latter. When refining the grid used in the slice simulations (doubling the number of cells in the spanwise direction), the results are **not affected**. It should be noted, finally, that in the experimental flow, there seem to exist corner vortices on the bump that raise some questions as to the validity of the experiments. Obviously, more work is needed.

## 6.1 Acknowledgments

This work was financed by the **DESider** project (Detached Eddy Simulation for Industrial Aerodynamics) which is a collaboration between Alenia, ANSYS-AEA, Chalmers University, CNRS-Lille, Dassault, DLR, EADS Military Aircraft, EURO-COPTER Germany, EDF, FOI-FFA, IMFT, Imperial College London, NLR, NTS, NUMECA, ONERA, TU Berlin, and UMIST. The project is funded by the European Community represented by the CEC, Research Directorate-General, in the 6th Framework Programme, under Contract No. AST3-CT-2003-502842.

## 7 REFERENCES

- [1] L. Davidson. Using isotropic synthetic fluctuations as inlet boundary conditions for unsteady simulations. *Advances and Applications in Fluid Mechanics*, 1(1):1–35, 2007.
- [2] R.H. Kraichnan. Diffusion by a random velocity field. *Physics of Fluids*, 13:22–31, 1970.
- [3] H. Le and P. Moin. Direct numerical simulation of turbulent flow over a backward facing step. Report no. TF-58, Stanford University, Dept. Mech. Eng., 1994.
- [4] P. Batten, U. Goldberg, and S. Chakravarthy. Interfacing statistical turbulence closures with large-eddy simulation. *AIAA Journal*, 42(3):485–492, 2004.
- [5] A. Smirnov, S. Shi, and I. Celik. Random flow generation technique for large eddy simulations and particle-dynamics modeling. *Journal of Fluids Engineering*, 123(2):359–371, 2001.
- [6] M. Billson, L.-E. Eriksson, and L. Davidson. Modeling of synthetic anisotropic turbulence and its sound emission. The 10th AIAA/CEAS Aeroacoustics Conference, AIAA 2004-2857, Manchester, United Kingdom, 2004, 2004.
- [7] M. Billson. *Computational Techniques for Turbulence Generated Noise*. PhD thesis, Dept. of Thermo and Fluid Dynamics, Chalmers University of Technology, Göteborg, Sweden, 2004.
- [8] S. Lee, S. Lele, and P. Moin. Simulation of spatially evolving turbulence and the application of Taylor’s hypothesis in compressible flow. *Physics of Fluids*, 4:1521–1530, 1992.
- [9] N. Jarrin, S. Benhamadouche, D. Laurence, and R. Prosser. A synthetic-eddy-method for generating inflow conditions for large-eddy simulations. *International Journal of Heat and Fluid Flow*, 27(4):585–593, 2006.
- [10] G. Byun, R.L. Simpson, and C. H. Long. A study of vortical separation from three-dimensional symmetric bumps. *AIAA Journal*, 42(4):754–765, 2004.
- [11] M. Klein, A. Sadiki, and J. Janicka. A digital filter based generation of inflow data for spatially developing direct numerical or large eddy simulations. *Journal of Computational Physics*, 186(2):652–665, 2003.
- [12] L. Davidson and S.-H. Peng. Hybrid LES-RANS: A one-equation SGS model combined with a  $k - \omega$  model for predicting recirculating flows. *International Journal for Numerical Methods in Fluids*, 43:1003–1018, 2003.
- [13] P. Emvin. *The Full Multigrid Method Applied to Turbulent Flow in Ventilated Enclosures Using Structured and Unstructured Grids*. PhD thesis, Dept. of Thermo and Fluid Dynamics, Chalmers University of Technology, Göteborg, 1997.
- [14] L. Davidson and M. Billson. Hybrid LES/RANS using synthesized turbulence for forcing at the interface. *International Journal of Heat and Fluid Flow*, 27(6):1028–1042, 2006.
- [15] L. Davidson and S. Dahlström. Hybrid LES-RANS: Computation of the flow around a three-dimensional hill. In W. Rodi and M. Mulas, editors, *Engineering Turbulence Modelling and Measurements 6*, pages 319–328. Elsevier, 2005.
- [16] G. Pailhas, P. Barricau, Y. Touvet, and J.C. Monnier. Turbulent separated flow through a channel with a bump (to be presented). In *EWA-UFAST workshop*, Prague, 2008.
- [17] M. Kuntz, F. Menter, and Y. Egorov. Definition of bump shape. DESider project, Deliverable D2.2-01, ANSYS-CFX, 2004.
- [18] C. Mocket, B. Grescher, T. Knacke, R. Perrin, J. Fan, and F. Thiele. Demonstration of improved DES methods for generic and industrial applications. In S.-H. Peng and W. Haase, editors, *Advances in Hybrid RANS-LES Methods*, Notes on Numerical Fluid Mechanics and Multidisciplinary Design (to appear). Springer Verlag, 2007.